

Supporting Information

Highly Ordered, Plasmonic Enhanced Inverse Opal Photonic Crystal For Ultrasensitive Detection Of SEB

Huijing Shen^{a,b,#}, Jialei Bai^{b,#}, Xudong Zhao^b, Beibei Lu^a, Dianpeng Han^b, Shuang Li^b, Kang Qin^b, Shuyue Ren^b, Yu Wang^b, Minglin Wang^a, Yujing Lian^{a,*}, Zhixian Gao^{b,*}, Yuan Peng^{b,*}

a. Country College of Food Science and Engineering, Shandong Agricultural University, Tai'an 271018, P. R. China

b. Tianjin Key Laboratory of Risk Assessment and Control Technology for Environment and Food Safety, Tianjin Institute of Environmental and Operational Medicine, Tianjin 300050, P. R. China

#These authors contributed equally to this work.

Corresponding author:

Y Lian: yujinglian@sdau.edu.cn;

Z. Gao: gaozhx@163.com;

Y. Peng: dalidao@139.com.

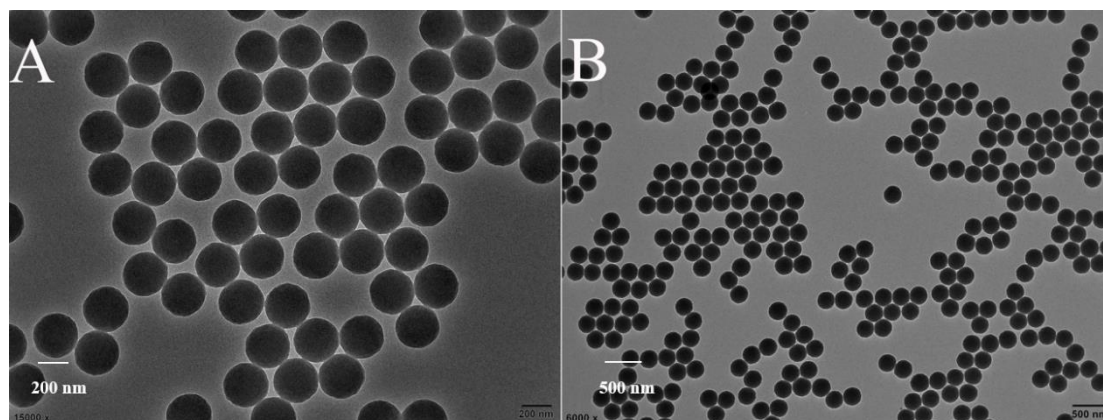


Figure S1. TEM image of the microscope of PMMA(Scale bar: A. 200 nm, B. 500 nm)

The PMMA microspheres possessed good morphology and uniform particle size, and the diameter of microspheres was about 270 nm.

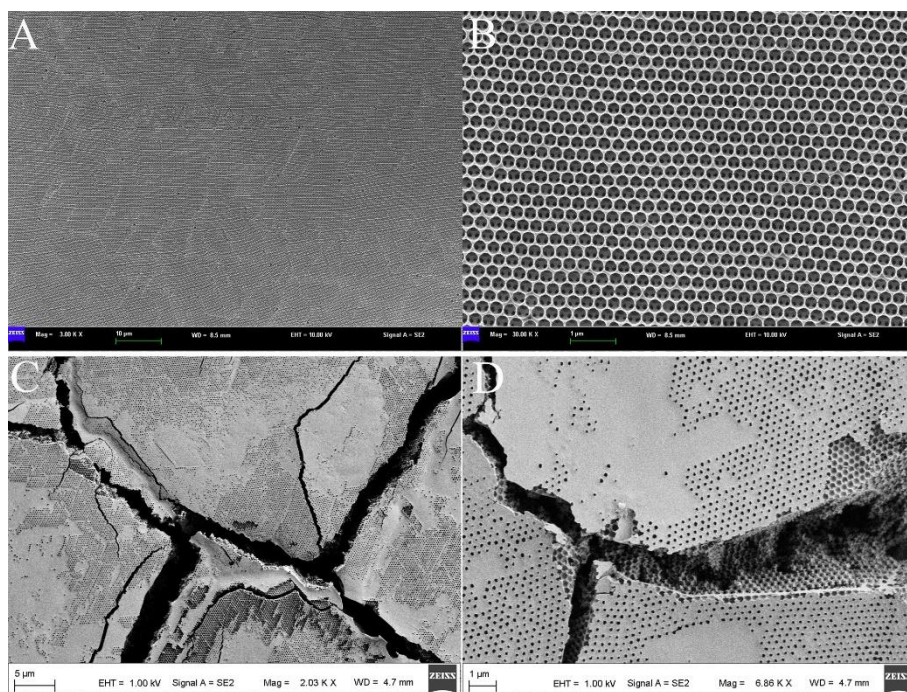


Figure S2. A-B. SEM of the SiO₂ IOPC obtained by co-assembly method after removing PMMA at 500 °C for 4 h (Scale bar: A. 10 μm, B. 1 μm). C-D. SEM of the SiO₂ IOPC obtained by sol-gel infiltration after removing PMMA at 500 °C for 4 h (Scale bar: C. 5 μm, D. 1 μm).

We adopted Hatton's co-assembly method to prepare highly ordered, crack-free inverse opal films,^{S1} and SEM showed the overall structure of the IOPC after high temperature calcination significantly reduced the number of defects during thermal annealing step and improved the quality of the structure. As comparison, IOPC was prepared through sol-gel infiltration method and calcined to remove PMMA as the same condition. The SEM results (Figure S2C, D) showed visible cracks and defects compared with Hatton's co-assembly method.

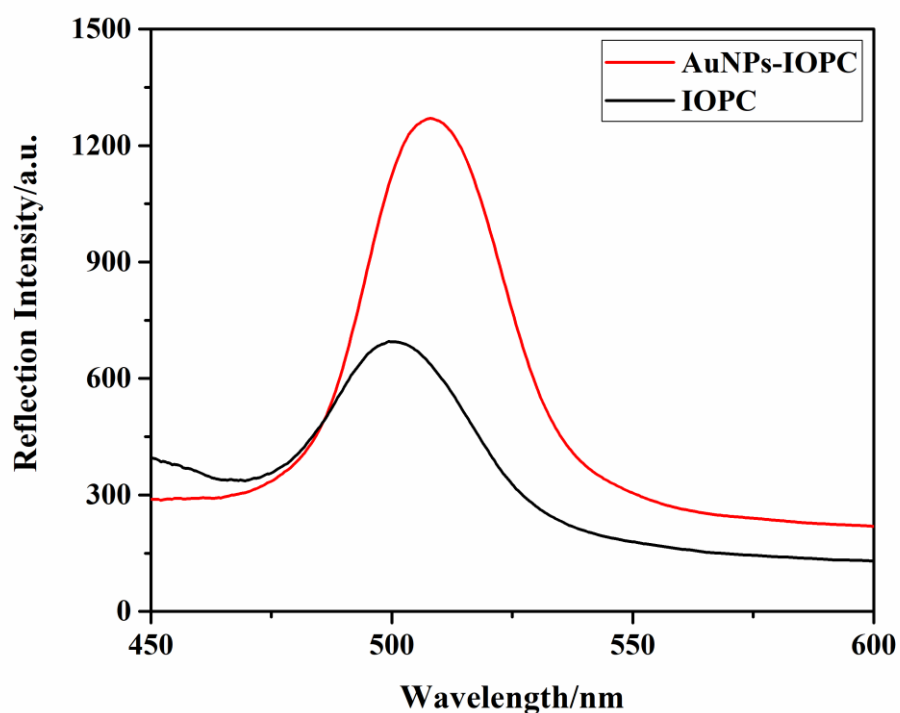


Figure S3. The reflection spectra of IOPC before and after modified by Au NPs

According to Figure S3, Au-IOPC produced enhanced peak intensity. The wavelength of the incident light was 515 nm, which was closed to the LSPR resonant wavelength shown in the UV–Vis absorption spectrum of the Au NPs and thus resulted in a strong LSPR effect. Thus, it proved that the introduction of Au NPs to IOPC could amplify the IOPC signal, leading to the improvement of the detecting sensitivity.

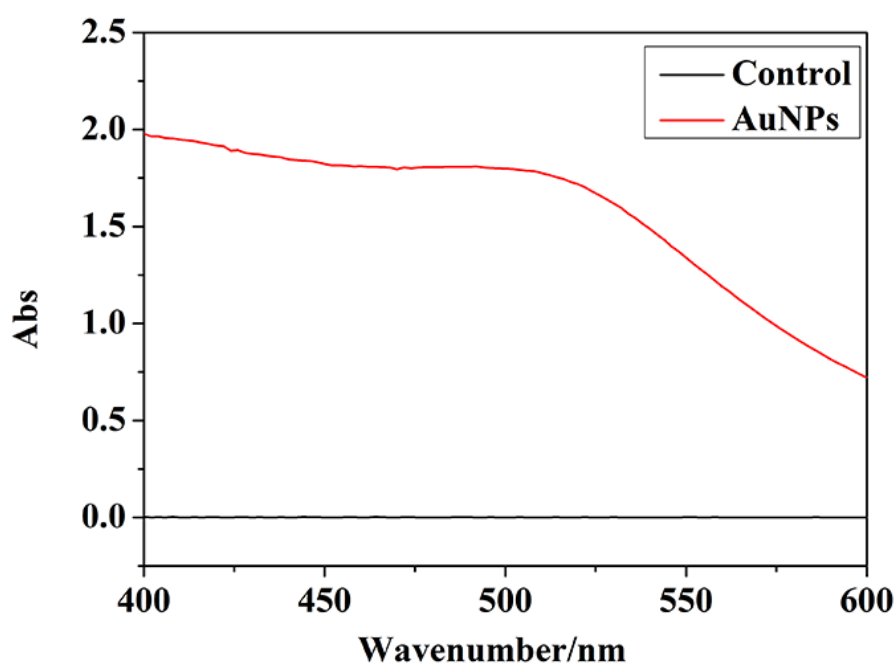


Figure S4. UV absorption spectra of Au NPs.

The maximum absorption wavelength of Au NPs was about 520 nm, which basically coincides with the photonic band gap (PBG) of IOPC.

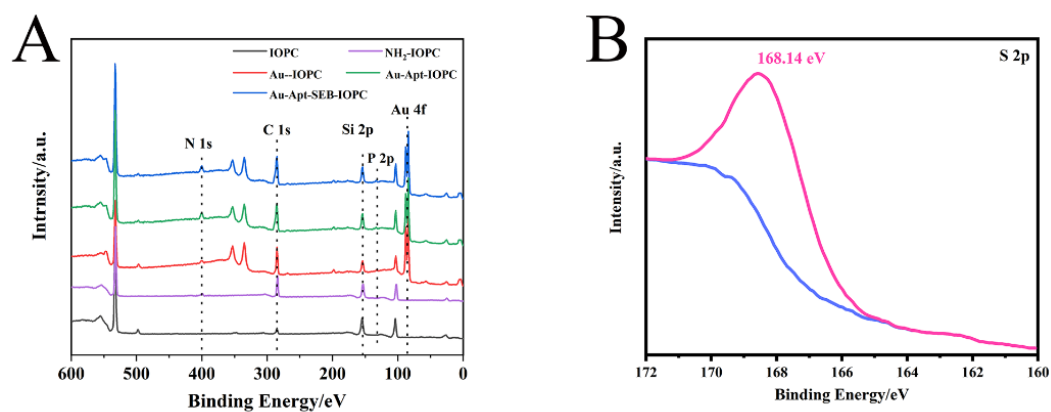


Figure S5. A. The X-ray photoelectron spectroscopy (XPS) of the IOPC, NH_2 -IOPC, Au-IOPC, Au-Apt IOPC, Au-Apt-SEB IOPC, B. The peak fitting of S2p.

The X-ray photoelectron spectroscopy (XPS, Escalab 250Xi) results further proved the successful modification of -NH_2 , Au NPs and aptamer (Figure S3). Compared with IOPC, NH_2 -IOPC had an obvious N peak at 400 eV, which indicated the successful introduction of amination.

Moreover, Au-IOPC had Au peak (BE = 87 eV), which indicated the Au NPs were successfully attached on the IOPC. After the aptamer was added on the surface of Au-IOPC, the appearance of P2p (BE = 133.08 eV) peak represented the existence of aptamer phosphate group, and S2p (BE = 168.14 eV) peak indicated the existence of mercapto group modified at the 5' end of the aptamer, which fully demonstrated the successful modification of the aptamer.

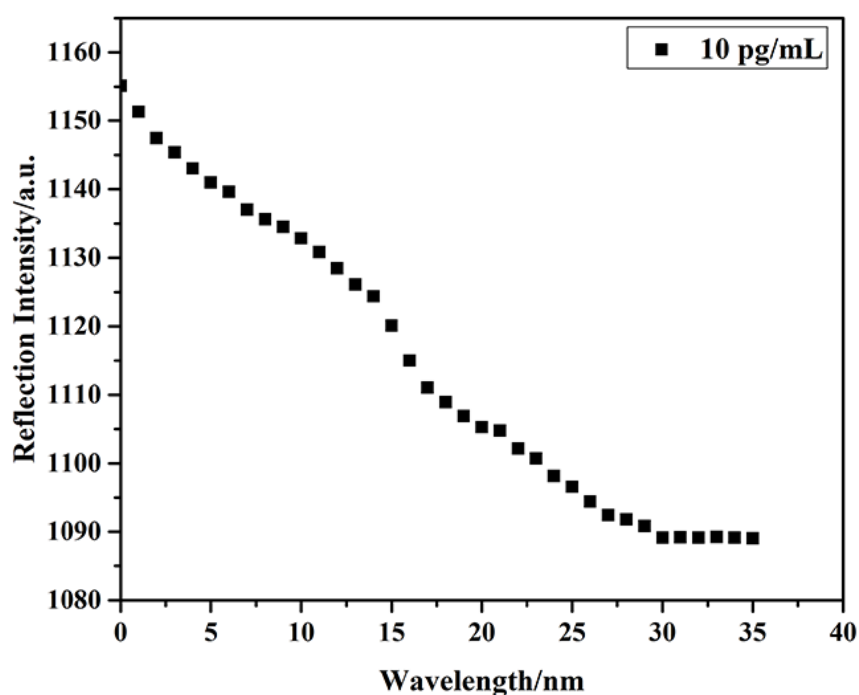


Figure S6. Kinetic response of the Au-Apt IOPC (10 pg mL^{-1})

The intensity of reflection peak was recorded every minute after SEB was added to the sensing system. As shown in Fig. S4, the peak intensity was continuously decreased, and after 30 minutes, it reached equilibrium. This indicated that the SEB detection could be completed in 35 min.

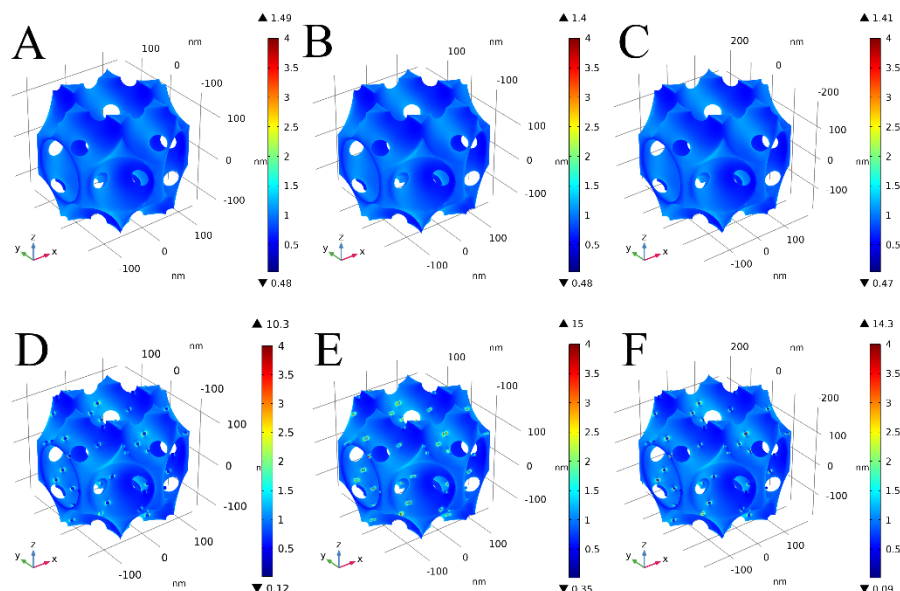


Figure S7. 3D model of simulated unit diagram of IOPC and Au-IOPC. IOPC (A. $d=165$ nm, $\lambda=435$ nm; B. $d=200$ nm, $\lambda=515$ nm; C. $d=255$ nm, $\lambda=590$ nm), Au-IOPC (D. $d=165$ nm, $\lambda=435$ nm; E. $d=200$ nm, $\lambda=515$ nm; F. $d=255$ nm, $\lambda=590$ nm).

The 3D model of unit diagram of IOPC and Au-IOPC was designed as Figure S7. The parameters used in 3D model was referred to the SEM results (Figure 2C). The periodic and scattering boundary conditions were used in the simulation. The reflection spectra was calculated through simulation, and the result (525 nm) was in close with experiment result (510 nm).

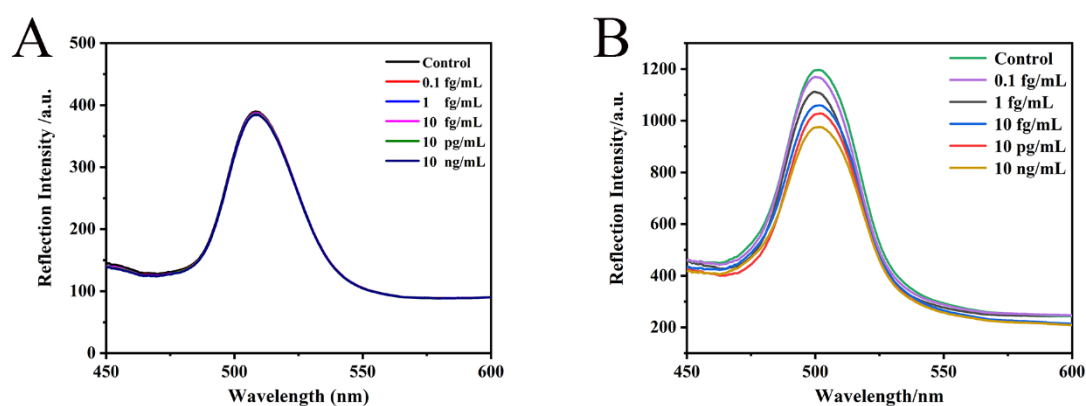


Figure S8. Reflection spectra of A) Au-IOPC and B) Au-Apt IOPC responding to SEB.

After the preparation of Au-IOPC, it was used to detect SEB. The Au-IOPC were immersed in deionized water and placed below the optical probe until the detecting system was stable. Then different concentrations of SEB were added, and corresponding reflectance spectrum were recorded.

Figure S8A showed that with the increasing of SEB concentration, the reflection spectrum of the Au-IOPC remained almost constant. Meanwhile, the Au-Apt IOPC was used to detect SEB as the same method, and the increasing SEB could cause decrease of the reflection peak intensity (Figure S8B). This phenomenon illustrated that IOPC without recognition element, aptamer, would not respond to the target, SEB. In other words, SEB could not non-specifically bind to the IOPC without aptamer.

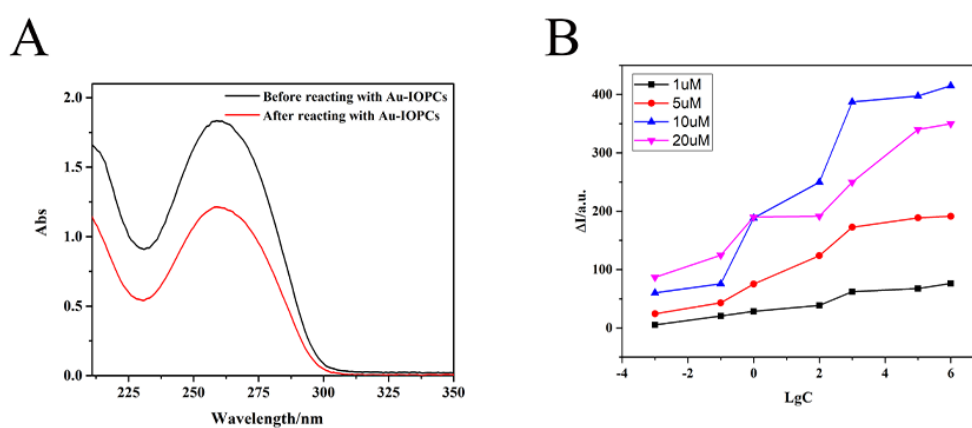


Figure S9. A. UV absorption spectra of the SEB aptamer before and after the reaction with Au-IOPC, B. Optimization of the SEB aptamer concentration reacted with Au-IOPC.

As shown in Figure S9A, after IOPC modification of aptamer, the UV absorption peak of Apt-IOPCs showed an obvious downward trend, and Au-IOPCs were successfully modified into aptamers. Under four SEB aptamer concentrations of 1 μ M, 5 μ M, 10 μ M and 20 μ M, the response of the inductive material to SEB was the strongest at 10 μ M aptamer concentration, and the intensity of the reflection peak decreased the most, and the response signal was significant (Figure S9B).

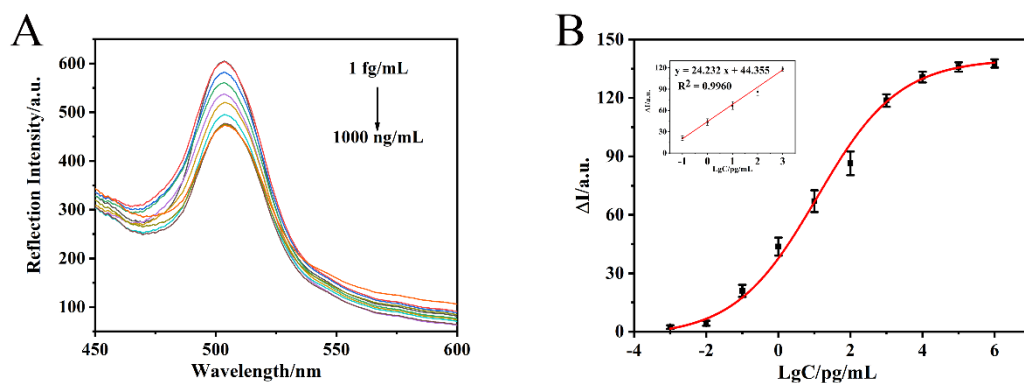


Figure S10 A. Optical responses of the CHO-IOPC to different SEB concentrations (from 1 fg mL⁻¹ to 1000 ng mL⁻¹); B. The standard curve of SEB detection (inset: linear relationship between the peak intensity changes and logarithm concentration of SEB). The averaged values and standard deviations were calculated from 3 replicated measurements.

CHO-Apt IOPC was used to detect SEB as a comparison. After SEB was added in the sensing system, the peak intensity also decreased gradually with the increasing concentration of SEB (Figure S10A). However, it showed linear relationship between ΔI and $\lg C$ at 10^{-1} – 10^3 pg mL⁻¹ (Figure S10B), and the regression equation is $y = 22.232x + 44.355$ with the $R^2 = 0.9960$. The LOD of CHO-Apt IOPC was 37.14 fg mL⁻¹.

The results showed that the preparation process of the Au-Apt IOPC was simpler than that of the traditional IOPC (CHO-Apt IOPC) without Au NPs, and the Au-Apt IOPC has higher sensitivity. This was because the introduction of Au NPs provided more binding sites, which increased the amount of the SEB aptamer fixed on the IOPC and improved the detection sensitivity. Therefore, the use of Au-Apt IOPC could achieve qualitative and ultra-sensitive quantitative detection of the target.

Table S1 Comparison of the as-proposed method with other existing assays for SEB detection

Methods	Materials	LOD	Linear range	Ref.
Fluorescent	Magnetic beads	0.269 pg mL ⁻¹	0.001–100 ng mL ⁻¹	S2
Chemiluminescence immunoassay	SiO ₂ microsphere	4 pg mL ⁻¹	0.01–1 ng mL ⁻¹	S3
Immunochromatography	AuNPs	10 pg mL ⁻¹	0.1–100 ng mL ⁻¹	S4
Electrochemistry	Triangular pyramid frustum nanostructure	0.17 ng mL ⁻¹	0.2–1000 ng mL ⁻¹	S5
SERS	Hollow gold nanospheres	0.001 ng mL ⁻¹	0.1 pg mL ⁻¹ –	S6

			1000 ng mL ⁻¹	
HPLC	—	0.5 µg mL ⁻¹	1–50 µg mL ⁻¹	S7
Chemiluminescence	Au NBPs	7.5 pg mL ⁻¹	10 pg mL ⁻¹ –100 ng mL ⁻¹	S8
Highly Ordered, Plasmonic Enhanced IOPC	IOPC and AuNPs	2.820 fg mL ⁻¹	10 ⁻² –10 ³ pg mL ⁻¹	This work

According to Table S1, although assays had been established to determine SEB, most of these methods were insufficient sensitivity, and the detection range was not wide.

(S1) Hatton, B.; Mishchenko, L.; Davis, S.; Sandhage, K. H.; Aizenberg, J., Assembly of Large-area, Highly Ordered, Crack-free Inverse Opal Films. *P. Natl. Acad. Sci. USA*. 2010, *107* (23), 10354-9.

(S2) Xu, Y. Y.; Huo, B. Y.; Li, C.; Peng, Y.; Tian, S.; Fan, L. X.; Bai, J. L.; Ning, B.; Gao, Z. X., Ultrasensitive Detection of Staphylococcal Enterotoxin B in Foodstuff through Dual Signal Amplification by Bio-barcode and Real-time PCR. *Food Chem*. 2019, *283*, 338-344.

(S3) Chen, L. L.; Zhang, Z. J.; Zhang, X. M.; Fu, A. H.; Xue, P.; Yan, R. F., A Novel Chemiluminescence Immunoassay of Staphylococcal Enterotoxin B using HRP-Functionalised Mesoporous Silica Nanoparticle As Label. *Food Chem*. 2012, *135* (1), 208-212.

(S4) Tarrisse, C. F.; Goulard-Huet, C.; Nia, Y.; Devilliers, K.; Marcé, D.; Dambrune, C.; Lefebvre, D.; Hennekinne, J. A.; Simon, S., Highly Sensitive and Specific Detection of Staphylococcal Enterotoxins SEA, SEG, SEH, and SEI by Immunoassay. *Toxins* 2021, *13* (2), 130.

(S5) Chen, X.; Shi, X.; Liu, Y.; Lu, L.; Lu, Y.; Xiong, X.; Liu, Y.; Xiong, X., Impedimetric Determination of Staphylococcal Enterotoxin B using Electrochemical Switching with DNA Triangular Pyramid Frustum Nanostructure. *Microchim. Acta* 2018, *185* (10), 460.

(S6) Hwang, J.; Lee, S.; Choo, J., Application of a SERS-based Lateral Flow Immunoassay Strip for the Rapid and Sensitive Detection of Staphylococcal Enterotoxin B. *Nanoscale* 2016, 8 (22), 11418-25.

(S7) Sospedra, I.; Marin, R.; Manes, J.; Soriano, J. M., Rapid Whole Protein Quantification of Staphylococcal Enterotoxin B by Liquid Chromatography. *Food Chem.* 2012, 133 (1), 163-166.

(S8) Zhao, Y.; Shi, L.; Miao, H.; Jing, X., "Add on" Dual-Modal Optical Immunoassay by Plasmonic Metal NP-Semiconductor Composites. *Anal. Chem.* 2021, 93 (6), 3250-3257.